Letter

When spin-orbit coupling meets local lattice distortions in Mott-like insulator iridates: The case of Sr_2IrO_4

A. Zafar,[1] M. Jakhar,[2] AM Milinda Abeykoon,[3] and V. Petkov[1,*]

[1]*Department of Physics, Central Michigan University, Mt. Pleasant, Michigan 48858, USA*
[2]*Inter-University Accelerator Center, Aruna Asaf Ali Marg, New Delhi 110067, India*
[3]*Photon Sciences Division, Brookhaven National Laboratory, Upton, New York 11973, USA*

(Received 1 April 2026; revised 8 June 2026; accepted 24 July 2026; published 12 August 2026)

Focusing on Sr_2IrO_4 as a model system, we investigate the poorly understood role of local lattice distortions in governing the unusual electronic properties of Mott-like insulating iridates. Using total x-ray scattering combined with structural modeling, we find no evidence for the previously proposed lowering of the average crystal symmetry. Instead, we uncover previously overlooked local lattice distortions that create two distinct IrO_6-octahedral layers already in the room-temperature paramagnetic insulating phase, thereby breaking the crystal symmetry locally rather than globally. Density functional theory calculations based on the experimentally determined structures show that the progressive strengthening of the local distortions with decreasing temperature may account for the enhanced band gap observed in the weakly ferromagnetic insulating phase. Our findings highlight the importance of local lattice distortions in shaping the electronic ground state of Sr_2IrO_4 and point to a broader role for hidden distortions and local symmetry breaking across Ir-based spin-orbit-coupled materials.

DOI: 10.1103/g3cv-g5zj

Introduction. Transition-metal (TM) oxides have long served as exemplary systems for exploring the interaction between lattice, charge, spin, and orbital degrees of freedom in correlated electron systems. In the first- and second-row transition series (3*d* and 4*d* oxides), strong electron-electron interactions and crystal-field effects give rise to a plethora of emergent phenomena, including high-temperature superconductivity in cuprates and colossal magnetoresistance in manganites. In contrast, the third transition series (5*d*) oxides present a unique case in the periodic table where the spatially extended 5*d* orbitals lead to decreased on-site Coulomb repulsion (Hubbard U) but significantly increased spin-orbit coupling (SOC). The competition between the two effects promotes unusual ground states that are not easily classified within the conventional Mott or band-insulator paradigms.

Among 5*d* TM oxides, iridates have emerged as particularly fascinating systems because key interactions—such as spin-orbit coupling, electron correlations, and crystal-field effects—occur on comparable energy scales [1–10]. A prototypical example is Sr_2IrO_4, where the octahedral crystal electric field (CEF) effects split the degenerate 5*d* orbitals into t_{2g} and e_g states and strong SOC further splits the t_{2g} manifold into two energy levels with effective angular momenta $J_{\text{eff}} = 1/2$ (doublet) and $J_{\text{eff}} = 3/2$ (quartet), forming narrow bands. Since the Ir^{4+} ions provide five 5*d* electrons, four of them fill the lower-energy $J_{\text{eff}} = 3/2$ band, and one electron partially fills the $J_{\text{eff}} = 1/2$ band where the Fermi level, E_f, resides. Effectively, this turns Sr_2IrO_4 into a half-filled band system that may be naively expected to show metallic behavior. Indeed, the isostructural compound Sr_2RuO_4 ($4d^5$) system is a Fermi liquid metal [11]. Unexpectedly, however, Sr_2IrO_4 ($5d^5$) is an insulator [8,12–21]. The current understanding is that this is because a moderate U is sufficient to split the narrow $J_{\text{eff}} = 1/2$ band and open a Mott-like gap supporting an insulating behavior. At this point, it is natural to consider that, largely, SOC determines the unusual ground state of Sr_2IrO_4. Theoretical and experimental studies [22–27], however, suggest that it is also strongly influenced by the material's highly adaptable crystal structure.

As is typical for 4*d* and 5*d* TM oxides of the Ruddlesden-Popper series $Sr_{n+1}TM_nO_{3n+1}$ (with $n = 1$), Sr_2IrO_4 consists of single layers of corner-sharing IrO_6 octahedra stacked along the *c* axis of a tetragonal lattice, where Sr atoms occupy the open space between the layers. Similar to Sr_2RuO_4, an *ideal* Sr_2IrO_4 may be expected to exhibit *I*4/*mmm* space group (S.G.) symmetry, in which the IrO_6 octahedra are elongated along the *c* axis of the crystal lattice but neither tilted nor rotated [28]. While such a structure may be stabilized at high pressure and temperature, room-temperature Sr_2IrO_4 adopts a tetragonal $I4_1/acd$ structure [29], where the octahedra are both elongated and exhibit antiphase rotations about the *c* axis (see Fig. 1). These rotations strongly influence the electronic properties of Sr_2IrO_4. In particular, the octahedral rotations allow the appearance of antisymmetric Dzyaloshinskii-Moriya interactions that induce spin canting leading to the appearance of a weak ferromagnetic (WFM) component in the nominally antiferromagnetic phase setting in below $T_1 = 240$ K [28–31]. Two additional magnetic

*Contact author: petko1vg@cmich.edu

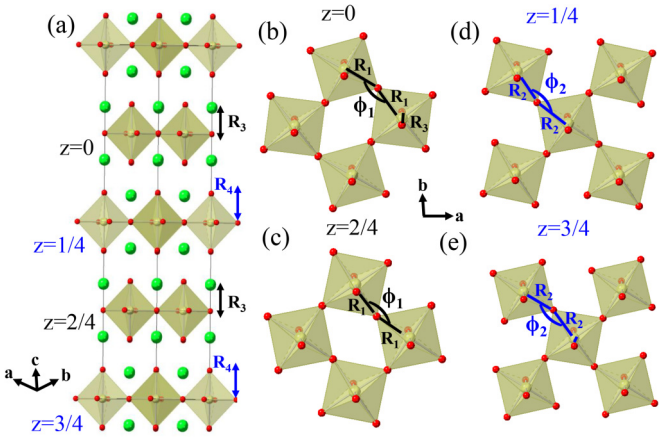

FIG. 1. (a) Crystal structure of perfect Sr_2IrO_4 with space group S.G. $I4_1/acd$ symmetry. The structure features layers of corner-sharing IrO_6 octahedra rotated about the tetragonal c axis by approximately 11° and Sr atoms positioned between the layers. The unit cell contains four layers positioned at $z = 0$, $z = 2/4$, $z = 1/4$, and $z = 3/4$, where all octahedra are the same. When the crystal symmetry is locally broken as described in the text, the layers positioned at $z = 0$ [panel (b)] and $z = 2/4$ [panel (c)] are built from IrO_6 units that are different from those building the layers positioned at $z = 1/4$ [panel (d)] and $z = 3/4$ [panel (e)]. Accordingly, in-plane Ir-O distances in the former, labeled as R_1, appear different from the in-plane Ir-O distances in the latter, labeled as R_2. The same pertains to the out-of-plane Ir-O distances R_3 and R_4. The in-plane Ir-O-Ir angles in the two sets of layers, labeled as, respectively, ϕ_1 and ϕ_2, also appear different. Sr, Ir, and O atoms are shown as green, dark yellow, and red circles.

phase transitions, attributed to spin-reorientation phenomena, are observed at $T_2 = 90$ K and $T_3 = 30$ K [see Fig. 2(a)]. Furthermore, the electrical resistivity, ρ, is also strongly affected, increasing in a highly nonmonotonic manner with decreasing temperature [Fig. 2(b)] in the WFM phase, where charge transport is believed to occur via hopping of carriers between neighboring Ir sites [32,33]. This hopping process depends sensitively on the Ir-O-Ir bond angles set by the octahedral rotations, as these angles control the overlap of t_{2g} orbitals (e.g., d_{xy} and d_{xz}) involved in the transport [2,34–41]. Pressure, chemical substitution, magnetic field, and electric field have been employed to tune the balance between SOC, electron correlations, and octahedral rotations in Sr_2IrO_4 [14–21], leading to a rich variety of nontrivial spin-orbit-entangled states that are distinct from the insulating phases observed in 4d oxides and are therefore challenging to understand. Further complicating the situation, recent harmonic generation [42], polarized neutron scattering [43], and magnetic torque measurements [44] suggest that the low-temperature states in Sr_2IrO_4 arise from an additional lowering of the average S.G. $I4_1/acd$ symmetry [24,25,45]. However, a lowering of the average crystal symmetry has not been conclusively established, hindering a microscopic understanding of the WFM phase and its anomalous electronic properties, including the nonmonotonic temperature dependence of the resistivity, ρ. Using total x-ray scattering combined with advanced structural modeling, we find no evidence for the previously proposed lowering of the average crystal symmetry. Instead, we uncover previously overlooked local lattice distortions that create two distinct IrO_6-octahedral layers already in the room-temperature paramagnetic (PM) insulating phase, thereby breaking the crystal symmetry locally rather than globally. The octahedral distortions become progressively stronger upon cooling and, as shown by density functional theory (DFT) calculations that explicitly account for them, may

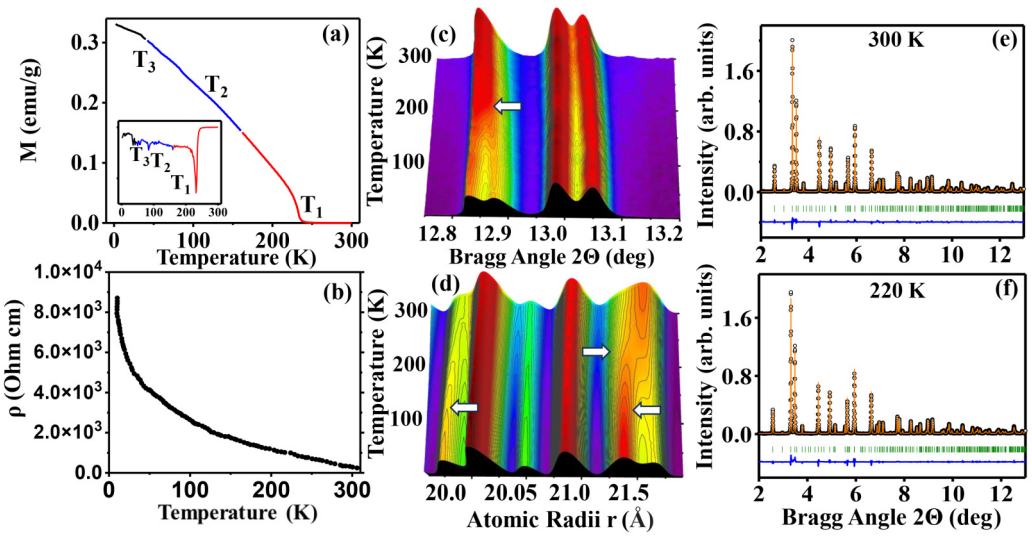

FIG. 2. (a) Magnetization, M, vs temperature. The inset shows its derivative, where negative dips indicate the presence of three magnetic phase transitions at about $T_1 = 240$ K, $T_2 = 90$ K, and $T_3 = 30$ K. (b) Temperature evolution of the resistivity adapted from Ref. [46]. (c) X-ray diffraction and (d) atomic PDF intensity-colored maps, where the intensity increases linearly as the color changes from violet to dark red. Arrows indicate the presence of nonlinearities in the temperature evolution of the diffraction patterns and PDFs taking place at T_1 and T_2. (e), (f) Rietveld fits (orange) to X-ray diffraction (XRD) patterns (black) obtained above and below the PM-WFM insulator phase transition. The fits are based on a perfect tetragonal S.G. $I4_1/acd$-type structure. The fit agreement factor is about 9%. The residual difference (blue) is shifted for clarity.

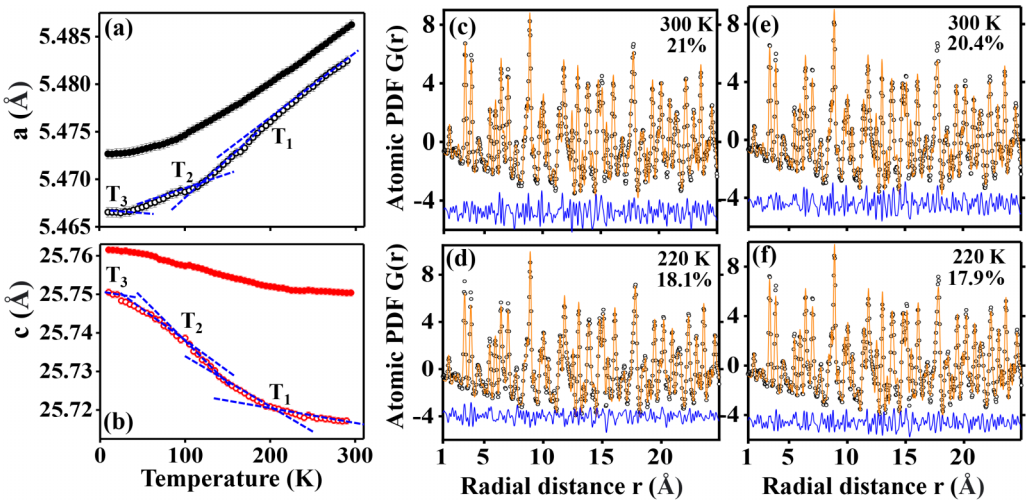

FIG. 3. (a), (b) Tetragonal lattice parameters, a and c, obtained by Rietveld fits (solid symbols) based on a perfect S.G. $I4_1/acd$-type structure. Lattice parameters obtained by PDF fits (open symbols) based on an S.G. $I4_1/acd$-type structure where the average tetragonal symmetry is locally broken are also shown. Broken lines emphasize the presence of inflection points in the temperature evolution of a and c at T_1, T_2, and T_3. (c)–(f) Fits (red) to PDFs (black) obtained below (220 K) and above (300 K) the PM-WFM insulator phase transition. The fits in panels (c) and (d) are based on a perfect S.G. $I4_1/acd$-type structure. The fits in panels (e) and (f) are based on a lower-symmetry S.G. $I4_1/a$-type structure that has been suggested to be adopted by the WFM insulating phase. Goodness-of-fit indicators are shown for each fit. Residual difference (blue) is shifted for clarity.

be responsible for the enhanced band gap of the WFM insulating phase. These results are consistent with recent studies of the magnetically ordered insulating phase in $BaIrO_3$ and Ba_2IrO_4, pointing to a broader principle in iridates: Local lattice distortions are not merely passive structural features but an important structural degree of freedom that strongly influence their electronic and magnetic ground states.

Results and discussion. Polycrystalline Sr_2IrO_4 was synthesized through a traditional two-step solid-state method, where stoichiometric amounts of $SrCO_3$ and IrO_2 fine powder were mixed, ground, calcined at 900 °C with a heating and cooling rate of 10 °C/min, and finally sintered at 1000 °C. Magnetic properties, shown in Fig. 2(a), were studied on a physical properties measurement system from Quantum Design. Data for ρ, shown in Fig. 2(b), are obtained from literature sources [46].

Total x-ray scattering experiments were conducted at the beamline 28-ID-1 at the NSLS-II, Brookhaven National Laboratory, using high-energy (74.46 keV) x-rays needed to obtain atomic pair distribution functions (PDFs) with good real-space resolution. Atomic PDF technique was employed because of its proven ability to characterize local lattice distortions in transition-metal oxides showing complex electronic ground states, including cuprates [47], manganates [48,49], and iridates [50]. The sample, packed into a Kapton tube, was kept inside a liquid helium cryostat used to control its temperature. The scattered x-ray intensities were collected from 300 to 10 K in steps of 5 K using a PerkinElmer area detector. XRD intensity-colored diffraction map is shown in Fig. 2(c). Intensity-colored map of atomic PDFs derived from the XRD patterns using software PDFgetX3 is shown in Fig. 2(d). In line with findings of independent studies [35,51], nonlinear changes in the maps at temperatures close to T_1, T_2, and T_3 indicate the presence of considerable spin-lattice interactions.

To investigate the temperature evolution of the average crystal structure, the experimental XRD patterns were subjected to Rietveld analysis using software FULLPROF [52]. Representative results from Rietveld fits based on an S.G. $I4_1/acd$ model (eight refinable parameters; see Table S1 in the Supplemental Material [53]) are shown in Figs. 2(e) and 2(f), and Fig. S1 of the Supplemental Material [53]. Refined tetragonal lattice parameters are shown in Figs. 3(a) and 3(b). The success of the fits confirmed that the sample is single tetragonal phase. To test the suggested lowering of the average crystal symmetry from S.G. $I4_1/acd$ to S.G. $I4_1/a$ [54], we also conducted Rietveld analysis based on the latter model (12 refinable parameters; see Table S1 in the Supplemental Material [53]), which features two types of Ir-O_6 octahedra in each of the layers in the unit cell. Results are shown in Fig. S2 of the Supplemental Material [53]. They are marginally better than those based on the S.G. $I4_1/acd$ model, providing insufficient evidence for a lowering of the average crystal symmetry in the WFM phase of Sr_2IrO_4.

To test crystal-symmetry-lowering hypothesis more rigorously, we fitted the experimental total PDFs using the same models. The refinements were carried out using the PDFgui software [55]. An advantage of PDF analysis over Rietveld refinement is that it incorporates both Bragg peaks and diffuse scattering contributions in the diffraction data—features observed in Sr_2IrO_4 in prior studies [29]—thereby making it sensitive to both the average crystal structure and local deviations from it. Representative fits based on the S.G. $I4_1/acd$ model are shown in Figs. 3(c) and 3(d), and Fig. S3 of the Supplemental Material [53]. The fits are of poor quality, indicating that the local crystal structure exhibits distortions that are not captured by the symmetry of the average structure. Despite having more refinable parameters, the lower average-symmetry S.G. $I4_1/a$ structural model did not yield a better

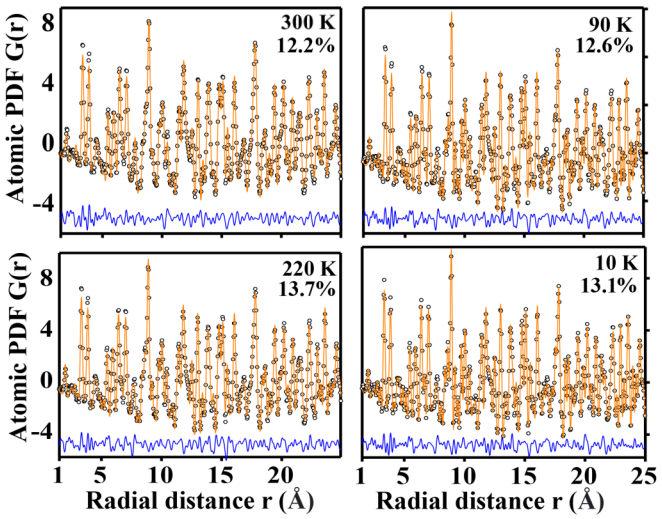

FIG. 4. Fits to PDFs (black) obtained below (220, 90, and 10 K) and above (300 K) the PM-WFM insulator phase transition. The fits are based on an S.G. $I4_1/acd$-type structure, where the average tetragonal symmetry is locally broken due to the presence of two distinct IrO_6-octahedral layers. Goodness-of-fit indicators are shown for each fit. Residual difference (blue) is shifted for clarity. The fits are superior to those shown in Figs. 3(c)–3(f) and Figs. S3 and S4 of the Supplemental Material [53].

fit to the PDF data [compare the data in Figs. 3(c) and 3(d), and Fig. S3 of the Supplemental Material [53] with those in Figs. 3(e) and 3(f), and Fig. S4 of the Supplemental Material [53]], providing no support for the suggested lowering of the average crystal symmetry. We tested several alternative structural models and found that the best description of the PDF data was provided by a model that preserves the average S.G. $I4_1/acd$ symmetry while permitting local symmetry breaking through decoupling the oxygen positions in the $z = 0$ and $z = 2/4$ layers from those in the $z = 1/4$ and $z = 3/4$ layers [Figs. 1(b)–1(e)]. Representative PDF fits are shown in Fig. 4. This local symmetry breaking gives rise to two types of IrO_6-octahedral layers, exhibiting significantly different basal (R_1, R_2) and apical (R_3, R_4) Ir-O bond lengths as well as different Ir-O-Ir bond angles. Notably, the locally symmetry-broken model is essentially different from the suggested average-symmetry-lowering S.G. $I4_1/a$ model. While the former features two distinct IrO_6-octahedral layers and requires only 10 refinable parameters, the latter introduces two inequivalent IrO_6 units within each layer and therefore necessitates a more complex structural description with 12 refinable parameters (Table S1 in the Supplemental Material [53]). Refined values for the lattice parameters, Ir-O-Ir bond angles, Ir-O bond distances, and octahedral layer-layer distances in the locally symmetry-broken S.G. $I4_1/acd$ model are shown in Figs. 3(a) and 3(b), and 5(a)–5(d). The distortion of IrO_6 octahedra in the distinct layers, computed as $D = 1/N \sum [(d_N - \langle d \rangle)/\langle d \rangle]^2$ [56,57], where $\langle d \rangle$ and d_N are the average and individual Ir-O bond distances in the respective octahedra $\langle N = 6 \rangle$, is shown in Fig. 5(e). As can be seen in the figure, the temperature evolution of the lattice parameters, bond distances, and angles exhibits clear inflection points at T_1, T_2, and T_3, revealing the particular structural features behind the observed nonlinearities in the experimental XRD and PDF data in the vicinity of three phase transitions exhibited by Sr_2IrO_4. Notably, the IrO_6 octahedra in the distinct layers are seen to increasingly suffer distortions, arising from the concurrent decrease and increase of the basal and apical Ir-O distances, respectively, with decrease of the temperature below T_1. Altogether, the results of PDF analysis show that the WFM phase of Sr_2IrO_4 precipitates from a structure state where the average tetragonal symmetry is already broken locally at room temperature, including the presence of two types of IrO_6-octahedral layers, where the two sets of Ir-O-Ir (Φ_1 and Φ_2) bond angles in the distinct layers deviate significantly from 180°, consistent with the observed insulating behavior.

The increase in ρ in the WFM phase then may be rationalized as follows. Because the on-site Coulomb repulsion is a local interaction, it is expected to vary only weakly

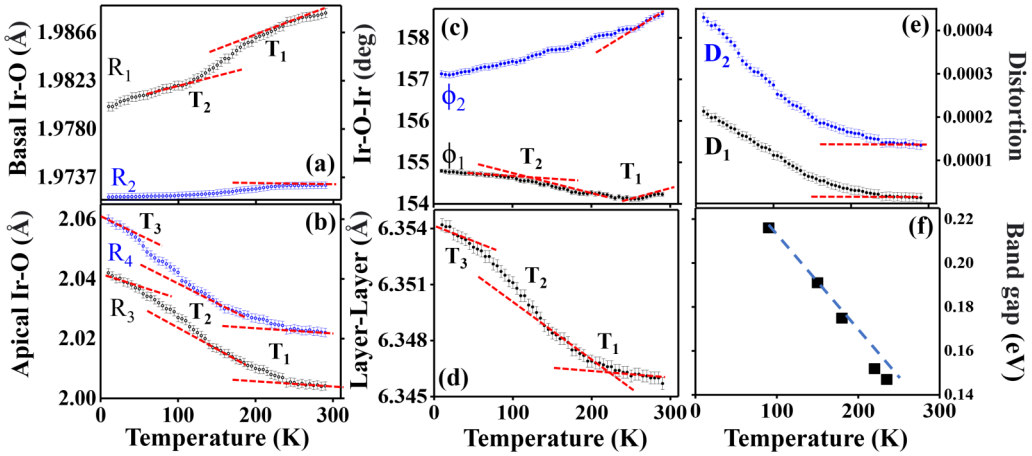

FIG. 5. Temperature evolution of (a) basal and (b) apical Ir-O bonds, (c) in-plane Ir-O-Ir bond angles, (d) distance between consecutive layers of IrO_6 octahedra, and (e) distortion of the octahedra in the two types of layers in Sr_2IrO_4. (f) Also shown are band gaps computed from PDF-fit refined structure data for an S.G. $I4_1/acd$ model where the crystallographic symmetry is locally broken. Note that the data shown in panels (a)–(e) are essentially different from those reported in Ref. [46], as the analysis in that work did not account for the presence of two distinct IrO_6-octahedral layers arising from the local breaking of the S.G. $I4_1/acd$ symmetry.

with temperature. Similarly, SOC is not expected to change significantly. Furthermore, since the Ir-O_2 planes in Sr_2IrO_4 remain well separated by rock-salt-type Sr-O layers [Fig. 1(a)] at all temperatures, charge transport in the WFM phase is expected to arise predominantly from carrier hopping between corner-sharing IrO_6 octahedra within these planes. Because the Φ_1 and Φ_2 bond angles—and thus the overlap of Ir-O t_{2g} orbitals in consecutive octahedral layers—change in opposite directions [Fig. 5(c)], the net effect of temperature-driven changes in the overall structural distortion on carrier hopping is likely limited. In contrast, the increased distortion of both types of IrO_6 octahedra/layers in Sr_2IrO_4 below T_1, arising from concerted changes in basal and apical Ir-O bond lengths [Figs. 5(a) and 5(b)] and locally broken crystal symmetry, is expected to significantly enhance CEF effects relative to the PM insulating phase, leading to further narrowing of the J_{eff} bands. This, in turn, would increasingly impede carrier hopping and drive the system toward a more insulating state in the WFM phase, as discussed in Refs. [58–63].

To validate our arguments, we performed DFT calculations, the details of which are provided in the Supplemental Material [53]. Consistent with previous DFT studies [22,69], fully relaxed calculations starting from the perfect $I4_1/acd$ structure [28] and incorporating both SOC and electron-electron correlation effects [with the Hubbard (U) parameter set to 1.75 eV, as recommended in Refs. [22,64]] yielded a narrow-gap insulating electronic structure (Fig. S5 of the Supplemental Material [53]). When the calculations were initiated from *locally symmetry-broken* $I4_1/acd$ structures obtained by us, the fully relaxed solutions converged to essentially the same nearly perfect tetragonal structure and corresponding electronic band structure shown in Fig. S5 of the Supplemental Material [53]. This behavior indicates that the experimentally observed locally symmetry-broken Sr_2IrO_4 structure, characterized by two distinct types of IrO_6-octahadral layers, cannot be reproduced within conventional zero-temperature DFT framework. To obtain a more realistic description of the evolution of the electronic structure with temperature, we performed DFT calculations based directly on the PDF-refined structures (Fig. 4) without further relaxation, thereby explicitly accounting for the observed local crystal-symmetry breaking. The resulting band structures are presented in Fig. S6 of the Supplemental Material [53], and the corresponding band gaps are summarized in Fig. 5(f). The calculations reveal a clear correlation between the magnitude of the local octahedral distortions and the size of the insulating gap: as the distortions become more pronounced with decreasing temperature, the band gap increases accordingly. This behavior provides a plausible explanation for the enhanced resistivity observed in the WFM insulating phase [Fig. 1(b)].

Interestingly, despite belonging to a different structural family, the Mott-like insulator $BaIrO_3$ exhibits analogous behavior. Upon cooling, distortions of inequivalent IrO_6 octahedra become increasingly pronounced and appear to be closely linked to the anomalous evolution of the electronic transport properties in the WFM insulating phase that emerges below 180 K [50]. Another example is tetragonal Ba_2IrO_4, which, like Sr_2IrO_4, consists of corner-sharing IrO_6 octahedra forming two-dimensional planes. The material undergoes a transition from a paramagnetic to a magnetically ordered Mott-like insulating state at approximately 240 K and exhibits a strongly nonlinear evolution of the electrical resistivity below this temperature [65]. Experimental and theoretical studies have suggested that the material develops increasingly pronounced local structural distortions upon cooling [66,67]. It is therefore plausible that these distortions give rise to distinct IrO_6 environments and associated local symmetry breaking that, analogous to that observed here in Sr_2IrO_4, enhances the band gap with decreasing temperature and contributes to its unusual transport behavior. Together with the present results, these earlier findings suggest that local symmetry breaking may be a common and important characteristic of iridates.

Concluding remarks. In summary, the unusual Mott-insulator-like ground state of Sr_2IrO_4 cannot be understood solely as a consequence of strong SOC and electron correlations; rather, it is inseparably linked to the presence of *local lattice distortions* that reshape the crystal-field landscape and significantly affect the bandwidth at low temperature. Far from being secondary perturbations, local lattice distortions in 5*d* transition-metal oxides, particularly iridates, act as local symmetry-breaking fields providing a control parameter that may play an important role in shaping their low-temperature electronic properties, ultimately enabling the emergence of nontrivial topological and multipolar states [68–72]. Any comprehensive description—or purposeful design—of ground states in 5*d* transition-metal oxides, in general, and iridates, in particular, must therefore include local lattice distortions as a fundamental degree of freedom.

Acknowledgments. This research was supported by the U.S. Department of Energy, Office of Science, Office of Basic Energy Sciences under Award No. DE-SC0021973 and used resources of the National Synchrotron Light Source at the Brookhaven National Laboratory provided by the DOE Office of Science under Contract No. DE-SC0012704. PARAM Rudra, a national supercomputing facility at Inter-University Accelerator Centre (IUAC), New Delhi, was used to obtain the DFT results presented in this paper. Thanks are due to R. Amin for the help with synchrotron experiments. A.Z., AMM.A., and V.P. performed the experiments. M.J. performed the DFT calculations. V.P. and A.Z. wrote the main manuscript text. All authors reviewed it.

The authors declare no competing interests.

Data availability. The data that support the findings of this article are openly available [73].

[1] F. Ye, C. Hoffmann, W. Tian, H. Zhao, and G. Cao, Pseudospin-lattice coupling and electric control of the square-lattice iridate Sr_2IrO_4, Phys. Rev. B **102**, 115120 (2020).

[2] E. M. Pärschke, W. C. Chen, R. Ray, and C. C. Chen, Evolution of electronic and magnetic properties of Sr_2IrO_4 under strain, npj Quantum Mater. **7**, 90 (2022).

[3] T. Shirakawa, H. Watanabe, and S. Yunoki, Theoretical studies of a three-band Hubbard model with a strong spin-orbit coupling for 5d transition metal oxide Sr_2IrO_4, J. Phys.: Conf. Ser. **454**, 012068 (2013).

[4] M. Nauman, T. Hussain, J. Choi, N. Lee, Y. J. Choi, W. Kang, and Y. Jo, Low-field magnetic anisotropy of Sr_2IrO_4, J. Phys.: Condens. Matter **34**, 135802 (2022).

[5] B. Hu, H. Zhao, Y. Zhang, P. Schlottmann, F. Ye, and G. Cao, Correlation between antiferromagnetic and Mott states in spin orbit coupled Sr_2IrO_4: A study of $Sr_2Ir_{1-x}M_xO_4$ (M = Fe or Co), Phys. Rev. B **103**, 115122 (2021).

[6] *Frontiers of 4D- and 5D-transition Metal Oxides*, edited by G. Cao and L. E. Delong (World Scientific, Singapore, 2013).

[7] Y. Du and X. Wan, The novel electronic and magnetic properties in 5*d* transition metal oxides system, Comput. Mater. Sci. **112**, 416 (2016).

[8] B. J. Kim, H. Ohsumi, T. Komesu, S. Sakai, T. Morita, H. Takagi, and T. Arima, Phase-sensitive observation of a spin-orbital Mott state in Sr_2IrO_4, Science **323**, 1329 (2009).

[9] R. E. Peierls, *Quantum Theory of Solids* (Oxford University Press, London, 1955).

[10] L. H. Greene, J. Thompson, and J. Schmalian, Strongly correlated electron systems—Reports on the progress of the field, Rep. Prog. Phys. **80**, 030401 (2017).

[11] T. E. Kidd, T. Valla, A. V. Fedorov, P. D. Johnson, R. J. Cava, and M. K. Haas, Orbital dependence of the Fermi liquid state in Sr_2RuO_4, Phys. Rev. Lett. **94**, 107003 (2005).

[12] B. J. Kim, H. Jin, S. J. Moon, J.-Y. Kim, B.-G. Park, C. S. Leem, J. Yu, T. W. Noh, C. Kim, S.-J. Oh, J.-H. Park, V. Durairaj, G. Cao, and E. Rotenberg, Novel $J_{\rm eff} = 1/2$ Mott state induced by relativistic spin–orbital coupling in Sr_2IrO_4, Phys. Rev. Lett. **101**, 076402 (2008).

[13] D. Haskel, G. Fabbris, M. Zhernenkov, P. P. Kong, C. Q. Jin, G. Cao, and M. Van Veenendaal, Pressure tuning of the spin-orbit coupled ground state in Sr_2IrO_4, Phys. Rev. Lett. **109**, 027204 (2012).

[14] G. Cao, J. Terzic, H. D. Zhao, H. Zhheng, L. E. De Long, and S. P. Riseborough, Electrical control of structural and physical properties via strong spin-orbit interactions in Sr_2IrO_4, Phys. Rev. Lett. **120**, 017201 (2018).

[15] G. Cao, A. Subedi, S. Calder, J.-Q. Yan, J. Yi, Z. Gai, L. Poudel, D. J. Singh, M. D. Lumsden, A. D. Christianson, B. C. Sales, and D. Mandrus, Hallmarks of the mott–hubbard transition in the optical response of Sr_2IrO_4, Phys. Rev. B **87**, 155136 (2013).

[16] I. N. Bhatti and A. K. Pramanik, Evolution of physical properties in hole doped Sr_2IrO_4: A $J_{\rm eff} = 1/2$ magnetic insulator, J. Phys.: Conf. Ser. **1086**, 012014 (2018).

[17] S. Chikara, O. Korneta, W. P. Crummett, L. E. DeLong, P. Schlottmann, and G. Cao, Lattice-driven magnetism in Sr_2IrO_4 studied by high-pressure x-ray diffraction, Phys. Rev. B **80**, 140407(R) (2009).

[18] A. de la Torre, S. McKeown Walker, F. Y. Bruno, S. Riccó, Z. Wang, I. Gutierrez Lezama, G. Scheerer, G. Giriat, D. Jaccard, C. Berthod, T. K. Kim, M. Hoesch, E. C. Hunter, R. S. Perry, A. Tamai, and F. Baumberger, Collapse of the Mott gap and emergence of a nodal liquid in lightly doped Sr_2IrO_4, Phys. Rev. Lett. **115**, 176402 (2015).

[19] D. Afanasiev, A. Gatilova, D. J. Groenendijk, B. A. Ivanov, M. Gibert, S. Gariglio, J. Mentink, J. Li, N. Dasari, M. Eckstein, Th. Rasing, A. D. Caviglia, and A. V. Kimel, Ultrafast spin dynamics in photodoped spin-orbit Mott insulator Sr_2IrO_4, Phys. Rev. X **9**, 021020 (2019).

[20] M. P. M. Dean *et al.*, Ultrafast energy- and momentum-resolved dynamics of magnetic correlations in the photo-doped Mott insulator Sr_2IrO_4, Nat. Mater. **15**, 601 (2016).

[21] D. Choi, C. Yue, D. Azoury, Z. Porter, J. Chen, F. Petocchi, E. Baldini, B. Lv, M. Mogi, Y. Su, S. D. Wilson, M. Eckstein, P. Werner, and N. Gedik, Light-induced insulator–metal transition in Sr_2IrO_4 reveals the nature of the insulating ground state, Proc. Natl Acad. Sci. USA **121**, e2323013121 (2024).

[22] C. Martins, M. Aichhorn, L. Vaugier, and S. Biermann, Reduced effective spin-orbital degeneracy and spin-orbital ordering in paramagnetic transition-metal oxides: Sr_2IrO_4 versus Sr_2RhO_4, Phys. Rev. Lett. **107**, 266404 (2011).

[23] Q. Huang, J. L. Soubeyroux, O. Chmaissem, I. N. Sora, A. Santoro, R. J. Cava, J. J. Krajewski, and W. F. Peck, Jr., Neutron powder diffraction study of the crystal structures of Sr_2RuO_4 and Sr_2IrO_4 at room temperature and at 10 K, J. Solid State Chem. **112**, 355 (1994).

[24] M. A. Subramanian, M. K. Crawford, R. L. Harlow, T. Ami, J. A. Fernandez-Baca, Z. R. Wang, and C. Johnston, Sr_2RhO_4 and Sr_2IrO_4: Structural and magnetic studies of 4*d* and 5*d* transition metal analogs of La_2CuO_4, Phys. C: Supercond. **235**, 743 (1994).

[25] F. Ye, S. Chi, B. C. Chakoumakos, J. A. Fernandez-Baca, T. Qi, and G. Cao, Magnetic and crystal structures of Sr_2IrO_4: A neutron diffraction study, Phys. Rev. B **87**, 140406 (2013).

[26] R. Kadono, M. Miyazaki, M. Hiraishi, H. Okabe, A. Koda, K. Amemiya, and H. Nakao, Direct observation of oxygen polarization in Sr_2IrO_4 by O K-edge x-ray magnetic circular dichroism, Phys. Rev. B **107**, L201122 (2023).

[27] G. Cao, J. Bolivar, S. McCall, J. E. Crow, and R. P. Guertin, Weak ferromagnetism, metal-to-nonmetal transition, and negative differential resistivity in single-crystal Sr_2IrO_4, Phys. Rev. B **57**, R11039 (1998).

[28] H. Wang, M. Marshall, Z. Wang, K. W. Plumb, M. Greenblatt, Y. Zhu, D. Walker, and W. Xie, Non-centrosymmetric Sr_2IrO_4 obtained under high pressure, Inorg. Chem. **62**, 2161 (2023).

[29] M. K. Crawford, M. A. Subramanian, R. L. Harlow, J. A. Fernandez-Baca, Z. R. Wang, and D. C. Johnston, Structural and magnetic studies of Sr_2IrO_4, Phys. Rev. B **49**, 9198 (1994).

[30] H. Kim, J. Bertinshaw, J. Porras, B. Keimer, J. Kim, J.-W. Kim, J. Kim, J. Kim, G. Noh, G.-Y. Kim, S.-Y. Choi, and B. J. Kim, $Sr_2IrO_4/Sr_3Ir_2O_7$ superlattice for a model two-dimensional quantum Heisenberg antiferromagnet, Phys. Rev. Res. **4**, 013229 (2022).

[31] I. V. Solovyev, V. Mazurenko, and A. A. Katanin, Validity and limitations of the superexchange model for the magnetic properties of Sr_2IrO_4 and Ba_2IrO_4 mediated by the strong spin-orbit coupling, Phys. Rev. B **92**, 235109 (2015).

[32] M. Ge, T. F. Qi, O. B. Korneta, D. E. De Long, P. Schlottmann, W. P. Crummett, and G. Cao, Lattice-driven magnetoresistivity and metal-insulator transition in single-layered iridates, Phys. Rev. B **84**, 100402(R) (2011).

[33] P. Sharma, S. Singh, K. Kuga, T. Takeuchi, and R. Bindu, Synthesis and structural link to the electronic and magneto-transport properties of spin–orbit Mott insulator Sr_2IrO_4, J. Phys.: Condens. Matter **34**, 435402 (2022).

[34] C. Bhandari, Z. S. Popović, and S. Satpathy, Electronic structure and optical properties of Sr_2IrO_4 under epitaxial strain, New J. Phys. **21**, 013036 (2019).

[35] G. Zhang and E. Pavarini, Multiorbital nature of doped Sr_2IrO_4, Phys. Rev. Lett. **131**, 036504 (2023).

[36] J. N. Nelson, C. T. Parzyck, B. D. Faeth, J. K. Kawasaki, D. G. Schlom, and K. M. Shen, Mott gap collapse in lightly hole-doped $Sr_{2-x}K_xIrO_4$, Nat. Comm. **11**, 2597 (2020).

[37] O. B. Korneta, T. Qi, S. Chikara, S. Parkin, L. E. De Long, P. Schlottmann, and G. Cao, and G., Electron-doped $Sr_2IrO_{4-\delta}$ ($0 \leqslant \delta \leqslant 0.04$): Evolution of a disordered $J_{\text{eff}} = 1/2$ Mott insulator into an exotic metallic state, Phys. Rev. B **82**, 115117 (2010).

[38] G. Jackel and G. Khaliullin, Mott insulators in the strong spin-orbit coupling limit: From Heisenberg to a quantum compass and Kitaev models, Phys. Rev. Lett. **102**, 017205 (2009).

[39] C. Lane, Y. Zhang, J. W. Furness, R. S. Markiewicz, B. Barbiellini, J. Sun, and A. Bansil, First-principles calculation of spin and orbital contributions to magnetically ordered moments in Sr_2IrO_4, Phys. Rev. B **101**, 155110 (2020).

[40] T. F. Qi, O. B. Korneta, L. Li, K. Butrouna, V. S. Cao, X. Wan, P. Schlottmann, R. K. Kaul, and G. Cao, Spin-orbit tuned metal-insulator transitions in single-crystal $Sr_2Ir_{1-x}Rh_xO_4$ ($0 \leqslant x \leqslant 1$), Phys. Rev. B **86**, 125105 (2012).

[41] B. Zwartsenberg, R. P. Day, E. Razzoli, M. Michiardi, N. Xu, M. Shi, J. D. Denlinger, G. Cao, S. Calder, K. Ueda, J. Bertinshaw, H. Takagi, B. J. Kim, I. S. Elfimov, and A. Damascelli, Spin-orbit-controlled metal–insulator transition in Sr_2IrO_4, Nat. Phys. **16**, 290 (2020).

[42] K. L. Seyler, A. de la Torre, Z. Porter, E. Zoghlin, R. Polski, M. Nguyen, S. Nadi-Perge, S. D. Wilson, and D. Hsieh, Spin-orbit-enhanced magnetic surface second-harmonic generation in Sr_2IrO_4, Phys. Rev. B **102**, 201113 (2020).

[43] J. Jeong, Y. Sidis, A. Louat, V. Brouet, and P. Bourges, Time-reversal symmetry breaking hidden order in $Sr_2(Ir, Rh)O_4$, Nat. Commun. **8**, 15119 (2017).

[44] H. Murayama, K. Ishida, R. Kurihara, T. Ono, Y. Sato, Y. Kasahara, H. Watanabe, Y. Yanase, G. Cao, Y. Mizukami, T. Shibauchi, Y. Matsuda, and S. Kasahara, Bond directional anapole order in a spin-orbit coupled Mott insulator $Sr_2(Ir_{1-x}Rh_x)O_4$, Phys. Rev. X **11**, 011021 (2021).

[45] L. Zhao, D. H. Torchinsky, H. Chu, V. Ivanov, R. Lifshitz, R. Flint, T. Qi, G. Cao, and D. Hsieh, Evidence of an odd-parity hidden order in a spin–orbit coupled correlated iridate, Nat. Phys. **12**, 32 (2016).

[46] I. N. Bhatti, R. Rawat, A. Banerjee, and A. K. Pramanik, Temperature evolution of magnetic and transport behavior in 5*d* Mott insulator Sr_2IrO_4: Significance of magneto-structural coupling, J. Phys.: Condens. Matter **27**, 016005 (2014).

[47] S. J. L. Billinge and T. Egami, Short-range atomic structure of $Nd_{2-x}Ce_xCuO_{4-y}$ determined by real-space refinement of neutron-powder-diffraction data, Phys. Rev. B **47**, 14386 (1993).

[48] S. J. L. Billinge, V. Petkov, T. Proffen, G. H. Kwei, J. L. Sarrao, S. D. Shastri, and S. Kycia, Charge inhomogeneities in the colossal magnetoresistant manganites from the local atomic structure, Mater. Res. Soc. Symp. Proc. **602**, 177 (2001).

[49] E. S. Bozin, M. Schmidt, A. J. DeConinck, G. Paglia, J. F. Mitchell, T. Chatterji, and S. J. L. Billinge, Understanding the insulating phase in colossal magnetoresistance manganites: Shortening of the Jahn-Teller long-bond across the phase diagram of $La_{1-x}Ca_xMnO_3$, Phys. Rev. Lett. **98**, 137203 (2007).

[50] V. Petkov, A. Zafar, M. Jakhar, A. M. Abeykoon, and Z. Hegedues, Local lattice distortions drive the transition of $BaIrO_3$ into a ferromagnetic insulator state, Sci. Rep. **15**, 44953 (2025).

[51] H. Zhang, L. Hao, J. Yang, J. Mutch, Z. Liu, Q. Huang, K. Noordhoek, A. F. May, J.-H. Chu, J.-W. Kim, P. J. Ryan, H. Zhou, and J. Liu, Comprehensive electrical control of metamagnetic transition of a quasi-2D antiferromagnet by *in situ* anisotropic strain, Adv. Mater. **32**, 2002451 (2020).

[52] J. Rodriguez-Carvajal, FULLPROF: A program for Rietveld refinement and pattern matching Analysis, in *Satellite Meeting on Powder Diffraction of the XV Congress of the IUCr* (Toulouse, France, 1990), Vol. 127.

[53] See Supplemental Material at http://link.aps.org/supplemental/10.1103/g3cv-g5zj for details of DFT calculations and results from Rietveld and PDF data analysis.

[54] D. H. Torchinsky, H. Chu, L. Zhao, N. B. Perkins, Y. Sizyuk, T. Qi, G. Cao, and D. Hsieh, Structural distortion-induced magnetoelastic locking in Sr_2IrO_4 revealed through nonlinear optical harmonic generation, Phys. Rev. Lett. **114**, 096404 (2015).

[55] C. L. Farrow, P. Juhas, J. W. Liu, D. Bryndin, E. S. Božin, J. Bloch, T. Proffen, and S. J. L. Billinge, PDFfit2 and PDFgui: Computer programs for studying nanostructure in crystals, J. Phys.: Condens. Matter **19**, 335219 (2007).

[56] J. S. Zhou and J. B. Goodenough, Universal octahedral-site distortion in orthorhombic perovskite oxides, Phys. Rev. Lett. **94**, 065501 (2005).

[57] J. Rodriguez-Carvajal, G. Rousse, C. Masquelier, and M. Hervieu, Electronic crystallization in a lithium battery material: Columnar ordering of electrons and holes in the spinel $LiMn_2O_4$, Phys. Rev. Lett. **81**, 4660 (1998).

[58] E. Paris, Y. Tseng, E. M. Pärschke, W. Zhang, M. H. Upton, A. Efimenko, K. Rolfs, D. E. McNally, L. Maurel, M. Naamneh, M. Caputo, V. N. Strocov, Z. Wangj, D. Casad, C. W. Schneider, E. Pomjakushina, K. Wohlfeld, M. Radovic, and T. Schmitt, Strain engineering of the charge and spin-orbital interactions in Sr_2IrO_4, Proc. Natl Acad. Sci. USA **117**, 24764 (2020).

[59] B. Kim, P. Liu, and C. Franchini, Dimensionality-strain phase diagram of strontium iridates, Phy. Rev. B **95**, 115111 (2017).

[60] D. Haskel, G. Fabbris, J. H. Kim, L. S. Veiga, J. R. L. Mardegan, C. A. Escanhoela Jr, S. Chikara, V. Struzhkin, T. Senthil, B. J. Kim, G. Cao, and J.-W. Kim, Possible quantum paramagnetism in compressed Sr_2IrO_4, Phys. Rev. Lett. **124**, 067201 (2020).

[61] Y. Li, R. D. Schaller, M. Zhu, D. A. Walko, J. Kim, X. Ke, L. Miao, and Z. Q. Mao, Strong lattice correlation of non-equilibrium quasiparticles in a pseudospin-1/2 Mott insulator Sr_2IrO_4, Sci. Rep. **6**, 19302 (2016).

[62] H. Watanabe, T. Shirakawa, and S. Yunoki, Theoretical study of insulating mechanism in multiorbital Hubbard models with a large spin-orbit coupling: Slater versus Mott scenario in Sr_2IrO_4, Phys. Rev. B **89**, 165115 (2014).

[63] H. Liu and G. Khaliullin, Pseudo-Jahn-Teller effect and magnetoelastic coupling in spin-orbit Mott insulators, Phys. Rev. Lett. **122**, 057203 (2019).

[64] H. Jin, H. Jeong, T. Ozaki, and J. Yu, Anisotropic exchange interactions of spin-orbit-integrated states in Sr_2IrO_4, Phys. Rev. B **80**, 075112 (2009).

[65] H. Okabe, M. Isobe, E. Takayama-Muromachi, A. Koda, S. Takeshita, M. Hiraishi, M. Miyazaki, R. Kadono, Y. Miyake, and J. Akimitsu, Ba_2IrO_4: A spin-orbit Mott insulating quasi-two-dimensional Antiferromagnet, Phys. Rev. B **83**, 155118 (2011).

[66] S. Moser, L. Moreschini, A. Ebrahimi, B. D. Piazza, M. Isobe, H. Okabe, J. Akimitsu, K. S. Kim V.Mazurenko, A. Bostwick, E. Rotenberg, J. Chang, H. Rønnow, and M. Grioni, The electronic structure of the high-symmetry perovskite iridate Ba_2IrO_4, New J. Phys. **16**, 013008 (2014).

[67] A. Subedi, Octahedral rotation instability in Ba_2IrO_4, arXiv:2512.23690.

[68] Y. Liu *et al.*, Anomalous high-energy waterfall-like electronic structure in 5*d* transition metal oxide Sr_2IrO_4 with a strong spin-orbit coupling, Sci. Rep. **5**, 13036 (2015).

[69] A. Ataei, G. Grissonnanche, M.-E. Boulanger, L. Chen, E. Lefrancois, V. Brouet, and L. Taillefer, Phonon chirality from impurity scattering in the antiferromagnetic phase of Sr_2IrO_4, Nat. Phys. **20**, 585 (2024).

[70] H. Kim *et al.*, Quantum spin nematic phase in a square-lattice iridate, Nature **625**, 264 (2024).

[71] J. Porras, J. Bertinshaw, H. Liu, G. Khaliullin, N. H. Sung, J.-W. Kim, S. Francoual, P. Steffens, G. Deng, M. Moretti Sala, A. Efimenko, A. Said, D. Casa, X. Huang, T. Gog, J. Kim, B. Keimer, and B. J. Kim, Pseudospin-lattice coupling in the spin-orbit Mott insulator Sr_2IrO_4 Phys. Rev. B **99**, 085125 (2019).

[72] S. Zhou, K. Jiang, H. Chen, and Z. Wang, Correlation effects and hidden spin-orbit entangled electronic order in parent and electron-doped iridates Sr_2IrO_4, Phys. Rev. X **7**, 041018 (2017).

[73] A. Zafar, High resolution x-ray diffraction datasets for Sr_2IrO_4, Harvard Dataverse, 2026, https://doi.org/10.7910/DVN/X1HPWA.